HHS Public Access

Author manuscript

ACS Nano. Author manuscript; available in PMC 2021 May 09.

Published in final edited form as:

ACS Nano. 2019 June 25; 13(6): 6605–6617. doi:10.1021/acsnano.9b00653.

Increasing the Efficacy of Stem Cell Therapy *via* Triple-Function Inorganic Nanoparticles

Fang Chen[†,‡], **Eric Ruike Zhao**[†], **Ghanim Hableel**[†], **Tao Hu**[§], **Taeho Kim**[†,‖], **Jingting Li**[⊥], **Natalia Isabel Gonzalez-Pech**[#], **David J. Cheng**[†], **Jeanne E. Lemaster**[†], **Yijun Xie**[‡,#], **Vicki H. Grassian**[†,#,¶], **George L. Sen**[⊥], **Jesse V. Jokerst**[*,†,‡,▽]

[†]Department of NanoEngineering, University of California, San Diego, 9500 Gilman Drive, La Jolla, California 92093, United States

[‡]Materials Science and Engineering Program, University of California, San Diego, 9500 Gilman Drive, La Jolla, California 92093, United States

[⊥]Department of Dermatology and Cellular and Molecular Medicine, University of California, San Diego, 9500 Gilman Drive, La Jolla, California 92093, United States

[#]Department of Chemistry and Biochemistry, University of California, San Diego, 9500 Gilman Drive, La Jolla, California 92093, United States

[▽]Department of Radiology, University of California, San Diego, 9500 Gilman Drive, La Jolla, California 92093, United States

[§]School of Materials Science and Engineering, Central South University, Changsha 410083, China

[‖]Department of Biomedical Engineering, Institute of Quantitative Health Science and Engineering, Michigan State University, 775 Woodlot Drive, East Lansing, Michigan 48824, United States

[¶]Scripps Institution of Oceanography, San Diego, 9500 Gilman Drive, La Jolla, California 92093, United States

[*]**Corresponding Author** jjokerst@eng.ucsd.edu. Tel.: +1 (858) 246-0896.

Author Contributions

F.C. and J.V.J. conceived the research, designed the experiments, and revised the manuscript thoroughly. F.C., E.Z., and G.H. performed the experiments. T.H. performed HRTEM and analyzed the results. T.K. helped with the *in vitro* and *ex vivo* MRI collection. J.L. and G.L.S. helped with the histology sample preparation and staining. J.E.L. helped with differentiation experiments. D.J.C. helped with data analysis. N.I.G. and V.H.G. helped with ICP-MS measurements. Y.X. performed the SQUID analysis. F.C. and J.V.J. wrote the manuscript.

The authors declare no competing financial interest.

ASSOCIATED CONTENT

Supporting Information

The Supporting Information is available free of charge on the ACS Publications website at DOI: 10.1021/acsnano.9b00653.

Size and PDI of MCF (Figure S1); characterizations of optimized MCF (Figure S2); STEM image and EDX mapping of SPIO-loaded MCF (Figure S3); EDX mapping and spectra of SIO under different reaction conditions (Figure S4); hysteresis loop of SIO (Figure S5); effect of labeling condition and half-life of nanoparticles inside hMSCs (Figure S6); SIO enters and labels hMSCs (Figure S7); MRI contrast of SIO (Figure S8); ultrasound contrast of SIO (Figure S9); MRI and US signal of SIO-labeled hMSCs (Figure S10); loading capacity of the MCF and SIO (Figure S11); no IGF release from IGF-loaded MCF (Figure S12); demonstration of SIO retention in mimicking tissues (Figure S13); *in vivo* study of SIO retention at the mouse heart apex by external magnet harness (Figure S14); retention of SIO-labeled hMSCs *versus* shear stress (Figure S15); growth of SIO-labeled hMSCs on the side wall (Figure S16); H&E staining of organs from four groups (Figure S17); change of LVEF for individual animals (Figure S18); radial strain analysis (Figure S19); effect of IGF-loaded SIO on the hMSC secretome (Figure S20) (PDF)

Abstract

Stem cell therapy in heart disease is challenged by mis-injection, poor survival, and low cell retention. Here, we describe a biocompatible multifunctional silica–iron oxide nanoparticle to help solve these issues. The nanoparticles were made *via* an *in situ* growth of Fe_3O_4 nanoparticles on both the external surfaces and pore walls of mesocellular foam silica nanoparticles. In contrast to previous work, this approach builds a magnetic moiety inside the pores of a porous silica structure. These materials serve three roles: drug delivery, magnetic manipulation, and imaging. The addition of Fe_3O_4 to the silica nanoparticles increased their colloidal stability, T_2-based magnetic resonance imaging contrast, and superparamagnetism. We then used the hybrid materials as a sustained release vehicle of insulin-like growth factor—a pro-survival agent that can increase cell viability. *In vivo* rodent studies show that labeling stem cells with this nanoparticle increased the efficacy of stem cell therapy in a ligation/reperfusion model. The nanoparticle-labeled cells increase the mean left ventricular ejection fraction by 11 and 21% and the global longitudinal strain by 24 and 34% on days 30 and 60, respectively. In summary, this multifunctional nanomedicine improves stem cell survival *via* the sustained release of pro-survival agents.

Graphical Abstract

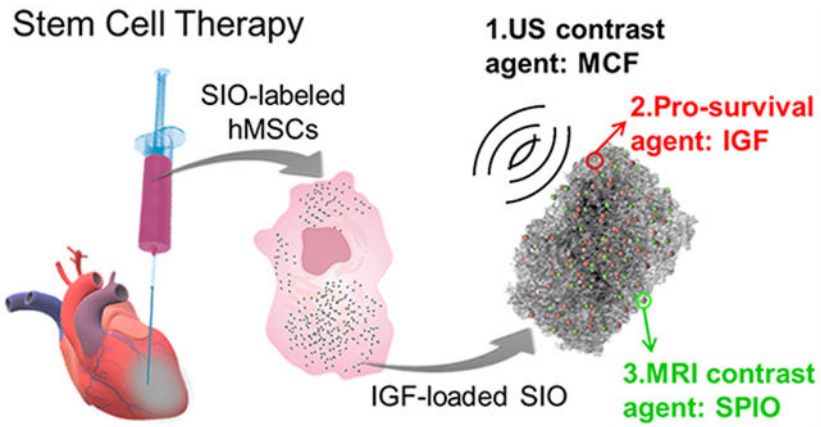

Keywords

mesoporous silica–iron oxide nanoparticles; contrast agents; theranostic nanoparticles; cell manipulation; stem cell therapy

Cardiovascular disease remains a leading cause of death[1] in part because human hearts have a limited regeneration capacity.[2] Consequently, many efforts have been made to regenerate/repair cardiac tissue *via* stem cells.[3–7] Mesenchymal stem cells (MSCs) are particularly promising due to their abundance, potent proliferation, multilineage differentiation capacity, and expression of paracrine factors.[8,9] There are three main mechanisms by which MSCs improve cardiac function: endogenous stem cell recruitment, replacement of apoptotic cells, and secretion of paracrine factors to increase proliferation and reduce inflammation.[10]

Unfortunately, stem cell therapy is limited by mis-injection into highly fibrotic tissues,[11] poor cell survival due to ischemia and inflammation,[7,12] and low cell retention in cardiac

tissue.[13] We and others[10,14–16] have used nanoparticles as imaging agents,[10] drug delivery vehicles,[15] and/or scaffolds[14] to improve stem cell therapy. Although various nanoparticles have shown potential in stem cell tracking,[10] pro-survival,[15] or manipulation,[16–19] translation has been limited by the customized utility of each particle type. Therefore, a hybrid multifunctional nanoparticle that can simultaneously track cells, deliver therapeutic drugs, and retain cells is highly desired.[20]

This work combines imaging, drug delivery, and cell directing capabilities into a single triple-function silica–iron oxide nanoparticle (SIO). This nanoparticle can guide cell injection in real time, track cells by multimodal imaging, increase viability, and increase cell retention by magnet manipulation (Figure 1). We have previously reported that mesocellular foam silica nanoparticles (MCF) could significantly increase the ultrasound contrast of human MSCs (hMSCs).[21] Here, we show that this foam-like structure can also offer sustained release of cargo to increase the survival of hMSCs. The same system can be coated with superparamagnetic iron oxide nanoparticles (SPIO) for magnetic resonance imaging (MRI) or manipulation of cells with an external magnet. The resulting product—called SIO here—increased the efficacy of stem cell therapy and improved heart function in a murine model of myocardial infarction. We also then evaluated its toxicity and the mechanism of myocardium repair.

RESULTS AND DISCUSSION

SIO Synthesis, Optimization, and Characterization.

SIO were made by growing SPIO *in situ* on MCF without any surface modification (Figure 2a). The MCF were chosen because they have good ultrasound contrast and great potential as a nanocontainer or reactor due to their relatively large pore size.[21–23] The MCF were fabricated *via* a bottom-up sol–gel micelle templating.[24] These silica particles became smaller and monodisperse after 8.5 h sonication (Figure S1).[25] The MCF we used to make SIO were 383 ± 167 nm (n = 570), and the diameter of the MCF pores was 16.6 ± 3.6 nm (n = 589) stacked in three dimensions (Figure S2).[24] These relatively large pores allow MCF to be reactive sites and to be loaded with proteins.

To make silica and iron oxide hybrid nanoparticles, we first tried to load SPIO directly to the MCF. This method is straightforward, but the preformed SPIO blocked the pores (Figure S3). This led to decreased drug loading. Thus, we developed an *in situ* growth method to achieve the goals: The SPIO were grown on both external surfaces and pore walls of MCF to form SIO. First, the MCF were dispersed in a solution of $FeCl_3$ and $FeCl_2$ in an ultrasonic bath. An alkaline solution that catalyzes the reaction was then added into this suspension with stirring, and iron oxide nanoparticles formed gradually on the surface and in the pores of MCF (Figure 2a). The MCF and liquid reactants were mixed well, so iron oxide nanoparticles could grow throughout the MCF instead of blocking the pores. In addition, the *in situ* growth method uses MCF as nanoreactors, which confined the growth of the SPIO in the pores of MCF. This confinement avoided the aggregation of SPIO even without surface modification of SPIO with organic molecules such as dextran, which is otherwise inevitable to prevent aggregation of the SPIO.[23]

Next, we optimized the conditions for *in situ* growth of SPIO. The SPIO growth needs alkali as a catalyst, but the silica can be dissolved by the alkali. The alkali concentration, type of cationic ions in the alkali, temperature, and reaction time are all important for iron oxide formation and silica dissolution. A lower pH and lower temperature decrease the extent of silica dissolution in alkali. Sodium ions and prolonged reaction time increase the magnetite crystal size, which increases the saturation magnetization.[26] Removing oxygen also improves the SPIO magnetization.[27] We investigated these factors and concluded that the optimal growth occurred at 1 h of reaction at room temperature in the presence of 0.5 M NaOH and nitrogen protection. The products made with the optimized reaction conditions showed good dispersity of iron in the MCF (Figure S4).

Energy-dispersive X-ray (EDX) mapping of a typical SIO showed that the iron was dispersed together with silicon and oxygen throughout the entire SIO (Figure 2b). SIO showed both crystal and amorphous regions under high-resolution transmission electron microscopy (HRTEM). The fast Fourier transformation (FFT) pattern in frame i of Figure 2c shows crystalline features with a lattice spacing of 2.97 Å, which agrees well with the lattice spacing of (220) planes of cubic Fe_3O_4 (2.966 Å on PDF #65–3170). In addition, this crystal region is a particle rather than a shell, which suggests that the SPIO were formed during the *in situ* growth. The FFT from frame ii (Figure 2c) indicates an amorphous structure typical of silica made with a low-temperature sol–gel method.[28] The distorted white centers of FFT patterns of both crystal and amorphous regions are due to objective stigmatism from magnetite (Figure 2c).[29]

The saturation magnetization of the SIO also proved that the iron oxide in the SIO was Fe_3O_4. The saturation magnetization of SIO at room temperature was 52 emu/g (Figure S5). According to the inductively coupled plasma mass spectrometry (ICP-MS) analysis, the Fe-to-Si mass ratio in SIO was 1.34. Therefore, the saturation magnetization of iron oxide in the SIO was 91 emu/g. The saturation magnetization indicated that the iron oxide in SIO was Fe_3O_4, whose saturation magnetization is 90 emu/g.[30] In addition, the small coercivity (0.1 Oe) and the shape of hysteresis loop (Figure S5) confirmed that the SIO are superparamagnetic.[31]

The SIO were irregularly shaped (Figure 2d), and their size distribution is shown in Figure 2e. Their average diameter was 380 ± 166 nm (n = 500), which is about the same as the starting MCF due to the balance between silica dissolution and SPIO deposition. The surface area, pore volume, and average pore size of MCF were 394 m^2/g, 0.50 cm^3/g, and 9.2 nm, respectively. With the alkali catalyst but no iron precursors, the pore volume and pore size were increased to 0.741 cm^3/g and 12.2 nm, which suggested dissolution of silica in the presence of alkali. The surface area, pore volume, and pore size of SIO were 333 m^2/g, 0.62 cm^3/g, and 9.2 nm, respectively, indicating the conjugation of SPIO on the MCF (Figure 2f).

The colloidal stability of SIO was also improved after SPIO conjugation. The colloidal stability was determined by measuring the absorbance of a nanoparticle suspension in a cuvette over time. Figure 2g shows that only 29% of the SIO settled after 24 h *versus* 49% of MCF that settled within 15 min at the same concentration. The increased colloidal stability may be due to the increased absolute zeta-potential value, which led to stronger electrostatic

repulsion between particles. Dynamic light scattering (DLS) results showed that zeta-potential of silica nanoparticles increased from −10 to 29 mV after deposition of positive SPIO.[32]

Cell Uptake of SIO.

Optimized SIO could be taken up by hMSCs without any transfection agents. SIO concentration and incubation time affected the cell uptake capacity. The cell uptake of SIO increased with the SIO labeling concentration ranging from 0 to 800 μg/mL (Figure S6a). We chose 200 μg/mL as the labeling concentration in order not to overdose the cells. The cell uptake of SIO reached a maximum at 4 h and decreased slightly afterward when 200 μg/mL of SIO was used (Figure S6b). The cell uptake of SIO at 4 h was 2.19 ± 0.34 ng/cell when the SIO labeling concentration was 200 μg/mL. This labeling condition was chosen for the late experiments unless specified.

The half-life of SIO in MSCs was studied *via* ICP analysis. The results showed that the cell uptake of SIO decreased exponentially *versus* time (Figure S6c). The half-life of SIO in hMSCs (passage 5) was 6.7 days, which was close to the doubling time of the cells—7.2 days. Therefore, the dilution of SIO in hMSCs may mainly be due to the division of cells.

Cell uptake of SIO was confirmed with transmission and fluorescence microscopy, iron staining, TEM image, and flow cytometry. Most of bright SIO in the transmitted image colocalized with the cells; fluorescence microscopy confirmed the nuclei (blue) and SIO (green) as shown in Figure S7a. Iron staining studies also showed the colocalization of iron (blue) and cells (pink) in the SIO-labeled cells, whereas there is no iron in the unlabeled cells (Figure S7b). The TEM image indicates that the SIO were taken up by hMSCs *via* phagocytosis, and the SIO maintained their shape (Figure S7c).[33] Flow cytometry analysis showed that approximately 93% out of 10 000 cells were labeled with SIO after 4 h of incubation (Figure S7d).

Biocompatibility of SIO.

We next measured the impact of SIO labeling on hMSCs. A resazurin assay showed the cell metabolism was 85.3% ($p = 0.00041$) and 98.5% ($p = 0.65$) of unlabeled cells when the SIO labeling concentration was 2 and 1 mg/mL SIO, respectively (Figure 3a). This indicates the excellent biocompatibility of the SIO. Cell counting experiments showed that the SIO did not inhibit the proliferation of hMSCs—the doubling times for SIO-labeled and unlabeled hMSCs were 3.6 and 3.7 days, respectively (Figure 3b). The shorter doubling time here than previously was likely due to the different cell batch and passage numbers. A calcein/ethidium homodimer III live/dead assay showed only 0.4% cell death after SIO labeling, which was negligible compared to the cell death of unlabeled cells, which is 0.2% (Figure 3c).

The impact of SIO labeling on phenotypes (CD73, CD90, and CD105)[34] was studied with flow cytometry (Figure 3d). Then 30 000 and 10 000 events were run for SIO-labeled and unlabeled hMSCs, and over 4500 cells were analyzed for all of the samples. We gated the fluorescence signals with unlabeled cells, and the gate was set where 99% of unlabeled cells

treated with antibodies were included. Results showed that 95.8, 95.8, and 97.3% of the SIO-labeled hMSCs maintained the CD73, CD90, and CD105 phenotypes.

SIO-labeled hMSCs retained their multipotency. Unlabeled and SIO-labeled hMSCs treated with adipogenic induction media were both stained red with Oil Red O, which indicates the presence of fatty lipid deposits in both cells. Also, both cells treated with osteogenic induction media were stained black by von Kossa staining, indicating the presence of calcium deposits (Figure 3e). Therefore, we could conclude that the SIO labeling did not affect the adipogenic and osteogenic differentiation capacities of hMSCs. Noticeably, the osteogenic-induced SIO-labeled hMSCs showed a calcium deposit heavier than that of the unlabeled cells (Figure 3e), which indicated that the SIO might enhance osteogenic differentiation similar to that of the reported silicate nanoplatelets.[35] However, this is unlikely to reduce the potential of SIO-labeled hMSCs in improving cardiac functions because SIO-labeled hMSCs did not differentiate into osteocytes in the absence of L-glutamine, ascorbate, β-glycerophosphate, and dexamethasone (Figure 3e).

The SIO-labeled cells could still move as seen in a migration assay (Figure 3f). For the unlabeled hMSCs, the cell density in the scratched area on day 3 was approximately 9290 cells/cm^2, which was 147% of the initial cell density in the unscratched area. For the SIO-labeled hMSCs, the cell density in the gap on day 3 was approximately 8871 cells/cm^2 or 143% of the initial cell density in the unscratched area. This result indicated that the SIO labeling did not inhibit cell migration.

Although SIO labeling showed no negative impact on metabolism, viability, proliferation, differentiation, phenotypes, and migration ability, it did affect the concentration of multiple cytokines in cell media. Secretome analysis showed a general increase in levels of cytokines with the addition of SIO: 50 out of 56 detected cytokines showed a slight increase of less than 1-fold upon the addition of SIO (Figure 3g). This is consistent with other nanoparticles.[10,36] The SIO-labeled hMSCs secreted 3.79-fold more IL1B, 2.93-fold more IL27, 2.47-fold more IL7, 2.04-fold more IL8, and 3.18-fold more MIP1B *versus* unlabeled cells; the changes are significant ($p < 0.05$ with a two-tailed homoscedastic *t* test were used). The addition of SIO led to significant decrease in TGFB secretion (0.36-fold of TGFB secreted by unlabeled hMSCs, $p < 0.05$ with two-tailed homoscedastic *t* test) (Figure 3g).

Functions of SIO—imaging, Sustained Release, and Cell Directing.

The *in situ* SPIO conjugation increased the nanoparticles' colloidal stability, zeta-potential, and saturation magnetization. These properties enable SIO to increase the efficacy of stem cell therapy through triple functions: enhancement of ultrasound and MRI contrast of cells, sustained release of pro-survival agents to increase cell viability, and magnetic-assisted manipulation of cells to improve retention.

First, SIO have high ultrasound and MRI contrast compared to soft tissues, which allows guided real-time injection through ultrasound imaging (Movie S1) and tracking of SIO-labeled cells *via* MRI.[10,37] We evaluated the T_2-based MRI signal of SIO with spin echo imaging. The limit of detection (LOD) of SIO with T_2-weighted MRI (7 T) was 43.7 μg/mL. The relaxivity per Fe was 32 ± 8.8 mM^{-1} s^{-1}, similar to commercial agents.[38] *In vivo* MRI

also showed a high contrast between SIO and myocardium (Figure S8). The ultrasound signal of SIO was tested with a 40 MHz transducer, and the LOD was 22.6 μg/mL (Figure S9). We then labeled hMSCs with SIO and scanned with MRI and ultrasound imaging. SIO increased both MRI and ultrasound contrast of hMSCs (Figure 4a) and could be used to count cells (Figure S10) down to 20 cells/μL *via* MRI and 152 cells/μL *via* ultrasound imaging. Therefore, the T_2-weighted MRI can exhibit excellent sensitivity for cell tracking that complements the excellent temporal resolution of ultrasound.[39]

The second function of SIO was drug delivery to enhance cell survival; enhanced cell survival can improve the therapeutic effects of MSCs for myocardial infarction.[12,40] Figure S11 shows that the SIO made with *in situ* growth method kept the high loading capacity of the MCF, which indicates that the pores were not blocked after *in situ* growth of the SPIO. The loading cargo was a protein—insulin-like growth factor (IGF, 7.6 kDa)—a pro-survival agent that can improve cell viability.[15] The IGF loading capacity of SIO was 7.36 mg/g, and the loading efficiency was greater than 98% when the IGF-to-nanoparticle mass ratio was 0.0075. The IGF loading capacity of SIO was only 1.2% lower than that of MCF (7.45 mg/g). Both nanoparticles had a similar linear dependence relationship between the loading capacity and IGF-to-nanoparticles ratio (Figure S11).

Moreover, SIO demonstrated better sustained IGF release ability than MCF. We were unable to detect any release from IGF-loaded MCF within 1 week *via* a bicinchoninic acid (BCA) assay (Figure S12). To confirm that we had loaded IGF in the first place, we mixed IGF-loaded MCF with the BCA solution and saw a high concentration of protein. We therefore concluded that MCF was unable to release IGF at detectable concentrations. This is likely due to strong electrostatic forces between the negatively charged MCF (−10 mV) and positively charged IGF at neutral pH.[41] On the other hand, SIO were positively charged (29 mV). We found that IGF-loaded SIO showed sustained release of IGF over 1 month (Figure 4b): 23.7, 34.8, and 45.1% of the loaded IGF was released on days 1, 7, and 29, respectively.

In vitro cell survival assays suggested the released IGF from SIO was still functional as a pro-survival agent. hMSCs were treated with IGF-loaded SIO, free IGF, free bovine serum albumin (BSA), incomplete media without fetal bovine serum (positive control), and complete media (negative control) for 1 week. To mimic cell transplantation, the cell media were not replaced with fresh media once cells were plated. The comparison between IGF and BSA groups indicated that IGF is a pro-survival agent for hMSCs.[15] Free IGF significantly increased the viability of hMSCs on days 1–4 but not on day 7 (Figure 4c). IGF-loaded SIO significantly increased the cell viability by 26, 57, and 53% on days 2, 4, and 7 *versus* incomplete media, underscoring the importance of sustained release. Furthermore, the viability of hMSCs treated with IGF-loaded SIO showed no significant (p = 0.09) decrease compared to complete media on day 7, suggesting that the sustained release of IGF from SIO increased the long-term survival of hMSCs.

The third function of SIO was to increase cell retention by magnet manipulation. We first investigated the retention of SIO with a magnet. First, an *in vitro* retention study showed that SIO stayed in static tissue mimics—0.5% agarose gel[42] attracted by a magnetic field (Figure S13). An *in vivo* study showed a significantly (p = 0.036, one-pair, type-two t test) higher

SIO retention in the left ventricle wall of mice with a magnet after 7 days. Approximately 15% of the SIO was detected in the hearts of mice with a magnet ($n = 9$), whereas no SIO were detected in those without a magnet ($n = 8$). The magnet was embedded in a jacket held close to the apex of the mouse, as shown in Figure S14. Seven days after injection, SIO were still visible in the left ventricle by *in vivo* MRI when a mouse was wearing a jacket with an external magnet, whereas most SIO were gone on day 7 compared to postinjection when a mouse was wearing a jacket without a magnet (Figure 4d). These results suggested that the SIO in the rodent myocardium could still be retained by an external magnet.

Next, we studied the effect of SIO labeling on cell retention by a magnet. The magnet-enhanced retention of SIO also increased the retention of SIO-labeled hMSCs. The retention of SIO-labeled hMSCs was 58.14% when the shear stress was 27 dyn/cm^2 (Figure 4e), which is higher than the mean wall shear stress of left ventricle of both mice and humans.[43] However, all unlabeled hMSCs were removed under the same conditions. We also quantitated the retention of cells *versus* shear stress from 7 to 35 dyn/cm^2 and found that the retention of SIO-labeled hMSCs decreased as the shear stress increased (Figure S15). The cell retention was approximately 85% when the shear stress was 12.8 dyn/cm^2, which is the mean wall shear stress in the human left ventricle.[44]

Further studies showed that suspended SIO-labeled hMSCs could overcome gravity and be attracted by an external magnet to the flask side wall. These attracted cells could adhere to and grow on the side wall. The cell density of SIO-labeled hMSCs with an external magnet was approximately 5850 cells/cm^2; otherwise, the cell densities were 0 cells/cm^2 (Figure 4f). After being attracted and adhered to the side wall, the SIO-labeled hMSCs could continue growing on the side wall without the magnet (Figure S16).

SIO-Labeled hMSCs Improve Left Ventricular Function.

In vivo experiments used the murine ischemia/reperfusion model in four groups: healthy control, negative control (no treatment), hMSC treatment, and IGF-loaded SIO-labeled hMSC treatment. Each group had 12 animals; this relatively large sample size provided over 97.8% power with one-sided 5% error to detect the improvement in left ventricular ejection fraction (LVEF) on day 60. The study timeline is shown in Figure 5a. Animals from the latter three groups received a 60 min ischemia by left anterior descending (LAD) coronary artery ligation followed by intramyocardial injection with 20 μL of media, 0.1 million hMSCs, or 0.1 million IGF-loaded SIO-labeled hMSCs, followed by reperfusion. Echocardiography[45] was used to evaluate the cardiac function on days 7, 30, and 60 after the surgery.

The treatment with stem cells was confirmed with immunofluorescence images. Only animals treated with stem cells, both unlabeled and SIO-labeled, showed the presence of CD73-PE, CD90-FITC, and CD105-APC (Figure 5b) in their left ventricles. In addition, iron staining, *ex vivo* MRI, and H&E staining showed that SIO only presented in the hearts from SIO-labeled hMSCs (Figure 5c,d). Moreover, the intramyocardial injection of hMSCs and SIO-labeled hMSCs did not change the pathology of other organs and showed no toxicity (Figure S17).

Echocardiography showed that unlabeled hMSCs decreased heart function on day 60 compared to the baseline. The hMSC control group had a decrease (−15%) in the mean LVEF on day 60 (Figure 6a); the mean change in LVEF of the hMSC control group was −17% on day 60, and there was no difference *versus* the negative control group (Figure 6b). This outcome is inconsistent with other reports; however, an inconsistent outcome of stem cell therapy in treating myocardial infarction is common in preclinical and clinical trials.[8] The inconsistency in outcomes with MSCs between studies may be due to the cell dosage, routes of administration, donor variance, culture expansion, and immunogenicity.[46,47] For example, most reported clinical trials with allogenic MSCs caused no significant changes in the LVEF, whereas most autologous MSCs increased the LVEF.[48]

On the other hand, IGF-loaded SIO-labeled hMSCs significantly improved the heart functions of mice with ischemia/reperfusion injuries. First, IGF-loaded SIO-labeled hMSC injection significantly improved the LVEF of diseased mice (Figure 6a). There were no significant differences between baseline LVEF among the diseased groups, which suggested that the model was consistent. The increases in mean LVEF were 11 and 21% on days 30 and 60, respectively. Changes in LVEF from baseline for individual animals in each group were also analyzed. Only 2 of 12 animals from the IGF-loaded SIO-labeled hMSC treatment group had a decrease in LVEF on day 60 compared to day 30, but this occurred in 6 of the 12 animals for the other three groups (Figure S18). The mean change in LVEF of the labeled hMSC treatment group on day 60 was 22%, which increased significantly compared to the negative control group.

IGF-loaded SIO-labeled hMSCs also significantly increased the global longitudinal strain (GLS)—an index of left ventricular (LV) systolic dysfunction.[49] There were no significant differences between baseline GLS among the diseased groups. The increase in GLS on days 30 and 60 was 24 and 34% compared to the baseline (Figure 6c). We also analyzed radial strain by dividing the LV myocardium into 49 nodes (Figure S19). Animals treated with IGF-loaded SIO-labeled hMSCs had an increased average radial strain in the nodes close to the apex on day 60 compared to day 30.

To further confirm this improvement, we studied the cardiomegaly by measuring the heart-to-body weight ratio and the pathological changes in the hearts. IGF-loaded SIO-labeled hMSC transplantation diminished cardiomegaly. The average heart-to-body weight ratios of the healthy control, the negative control, the hMSC control, and IGF-loaded SIO-labeled hMSC treatment groups were 5.7 ± 0.7, 8.2 ± 2.0, 8.6 ± 0.8, and 7.1 ± 0.8 mg/g, respectively (n = 12 for all groups) (Figure 6d,e). IGF-loaded SIO-labeled hMSC transplantation decreased the cardiomegaly by 43% (p = 0.041) compared to the negative control group.

Heart slices were stained with trichrome staining for fibrosis analysis. Figure 6f shows a representative heart slice from each group, and fibrosis tissues (blue) were seen from the slices of all diseased groups. We quantified six random hearts from each group, and each heart was sectioned to 10 μm with every 10th section collected. We analyzed 4–13 slices for each group and calculated the percentage of fibrosis with four continuous slices that showed a maximum fibrosis and a coefficient of variation less than 15%. The average percentages of fibrosis for the negative control, the hMSC control, and the labeled hMSC treatment groups

were 19.2 ± 9.0, 18.7 ± 12.1, and 14.6 ± 3.9% (Figure 6g), respectively. Therefore, IGF-loaded SIO increased the efficacy of stem cell therapy in treating ischemia/reperfusion injuries in mice.

All measurements including echocardiography, heart-to-body weight ratio, and pathological change showed that the IGF-loaded SIO labeling improved the stem cell treatment efficacy, which indicates the functionality of the SIO. Stem cells may improve the LVEF due to the paracrine factors, recruitment of autologous cells, and decreasing apoptosis of the local cells. Although the IGF-loaded SIO-labeled hMSCs increased the LVEF, without the hMSCs, the particles alone are unlikely to improve the LVEF because they cannot mediate the local paracrine factors, which has been proven by Roell *et al.*[50]

Hence, another mechanism for this improved stem cell therapy efficacy is likely due to the increased cytokine levels causing by nanoparticle labeling. We compared the secretome of IGF-loaded SIO-labeled hMSCs to unlabeled hMSCs. A general increase in levels of cytokines was seen with the addition of IGF-loaded SIO including many proteins broadly implicated in cardiac regeneration such as vascular endothelial growth factor, hepatocyte growth factor, basic fibroblast growth factor, stem cell factor, and monocyte chemotactic protein-1 (Figure S20). IGF-loaded SIO labeling significantly decreased the secretion of transforming growth factor beta (TGFB) to 22% ($p < 0.05$ when two-tailed homoscedastic t tests were used), which is beneficial because TGFB stops the cell cycle and leads to apoptosis.[51] Noticeably, although the SIO-only-labeled hMSCs secreted significantly more pro-inflammtory cytokines than unlabeled hMSCs, the IGF loading decreased this undesired effect caused by the SIO (Figure 3g and Figure S20).

CONCLUSIONS

We prepared a superparamagnetic mesocellular foam silica–Fe_3O_4 nanoparticle *via* an *in situ* growth method. The *in situ* SPIO conjugation increased the nanoparticles' colloidal stability, zeta-potential, magnetization, and sustained release profile for IGF. The optimized SIO allowed the enhancement of ultrasound and MRI contrast of cells, sustained release of pro-survival agents to increase cell viability, and magnet-assisted manipulation of cells to improve retention. Moreover, these nanoparticles changed the cytokine levels and improved the efficacy of stem cell therapy. Although this structure does not directly report viability, both echocardiography and histology studies showed that SIO loaded with IGF increased the efficacy of stem cell therapy in treating ischemia/reperfusion injury in mice. This could be improved by studies that correlated an exogenous agent such as the nanoparticles described here *versus* a reporter gene known to report viability.

MATERIALS AND METHODS

Poly(ethylene glycol)-*block*-poly(propylene glycol)-*block*-poly-(ethylene glycol) (P123), hexadecyltrimethylammonium bromide (CTAB), mesitylene, tetraethyl orthosilicate (TEOS), iron(II) chloride hexahydrate, and ammonium hydroxide were purchased from Sigma-Aldrich. Hydrochloric acid (HCl) was purchased from J.T. Baker. Ammonium

fluoride (NH_4F) was purchased from Acros Organics. Iron(III) chloride tetrahydrate was purchased from Fisher Chemical.

MCF Fabrication.

MCF were fabricated *via* a combination of micelle-templated sol–gel[24] and sonication gradient centrifugation methods.[25] First, HCl (90 mL, 1.6 M) was added to P123 (2.4 g) and stirred until the polymer was fully dissolved. Then, CTAB (400 mg), NH_4F (25 mg), and mesitylene (1.6 mL) were added followed by stirring at 700 rpm for 2 h. Next, TEOS (5.5 mL) was added dropwise with stirring at 1000 rpm followed by another 5 min of stirring. The mixture was then allowed to stand without stirring at 38 °C for 18 h. The products were collected and washed three times with ethanol followed by calcination (in a KSL-1100X furnace by MTI Corporation) at 600 °C for 5 h. To make MCF and optimize their size distribution, calcined particles were ground, sonicated for 2 h, and then centrifuged at 500 rpm for 5 min. The supernatant was collected and centrifuged at 1000 rpm for 5 min. Again, the supernatant was collected and centrifuged at 8000 rpm. Optimized MCF in the pellet were collected, lyophilized, and stored for later use.

SIO Synthesis.

SIO were made by growing SPIO onto the MCF *in situ*. First, Millipore water (resistivity >18.2 ohms) (1 mL) deoxygenated by N_2 bubbling was added to MCF (120 mg). Next, iron(III) chloride tetrahydrate (432 mg) and iron(II) chloride hexahydrate (159 mg) were added to the mixture. The vials were sealed, and N_2 was bubbled through once more followed by sonication for 5 min. Then, the catalyst sodium hydroxide (12 mL, 0.5 M) was added dropwise under vigorous stirring followed by stirring for another hour at room temperature. The nanoparticles were collected and centrifuged at 10 000 rpm for 10 min. Free iron oxide nanoparticles, which were small and stayed in the supernatants, were removed by removing the supernatants. The pellet was then suspended and washed with Millipore water. The centrifugation and washing processes were repeated twice more.

Characterization.

TEM images were taken on a conventional TEM (JEOL1400-Plus). High-resolution imaging was conducted on a HRTEM (FEI Tecnai F20) operated at 200 kV. The objective lens astigmatism of the HRTEM (FEI Tecnai F20) was corrected by using a standard carbon grating replica with Au/Pd particles. The live FFT pattern obtained from the amorphous carbon film was seen by tuning the ring. A nearly perfect round ring was obtained, indicating the reduction of astigmatism. We then saved the objective lens parameters (deflection currents). Subsequently, the SIO TEM samples were loaded and characterized. The element mapping of the SIO was performed on this HRTEM in scanning TEM (STEM) mode. During the optimization of reaction conditions, *Z*-contrast images and EDX spectra were taken on a STEM (Hitachi HD-2000) equipped with EDS detector (Bruker Quantax) at an accelerating voltage of 200 kV.

DLS measurements were obtained using a Malvern ZS 90 (Malvern Instruments). The absorbance was measured over time on a UV–vis spectrometer (SpectraMax from Molecular Devices) for colloidal stability evaluation. The nitrogen adsorption–desorption analysis was

done at 77 K on a Micromimetics ASAP 2020 system. Magnetic hysteresis loops were measured by sweeping the field from −7 to 7 T at 300 K on a Quantum Design MPMS3 superconducting quantum interface device (SQUID) magnetometer.

IGF Loading and Release from SIO.

IGF was loaded to SIO by mixing SIO (16 mg) and IGF (100 μL, 1 μg mL^{-1}) in Millipore water and stirring in an ice water bath in the dark for 18 h. The particles were then centrifuged at 8000 rpm for 5 min followed by washing with water three times. The supernatant was collected, and the amount of IGF remaining in the supernatant was measured by BCA assay. The loading capacity and efficiency were then calculated based on this result. A negative control was performed without nanoparticles. The IGF-loaded SIO were then lyophilized, refrigerated, and used within 7 days.

For the release study, IGF-loaded SIO (2 mg) were suspended in phosphate-buffered saline (PBS, 100 μL) preheated to 37 °C. The release system was sealed and rotated in a 37 °C oven. At designated time points, the nanoparticles were centrifuged at 14 000 rpm for 5 min, and the supernatant was collected. The pellet was then resuspended in fresh preheated PBS (100 μL).

Cell Culture and Labeling.

The hMSCs (PT-2501, Lonza) were seeded at 5000 cells cm^{-2} in mesenchymal stem cell growth media (PT-3001, Lonza) in an incubator with standard cell culture conditions. Cells used for SIO biocompatibility experiments were between passage 2 and passage 6. Cells used for MRI and ultrasound imaging were between passage 6 and passage 10. Cells for animal injections were passage 5 with the same lot number. Medium was changed every 3–4 days, and cells were passaged every 5–8 days at around 90% confluence using Trypsin-EDTA (0.25%, Gibco). All cells were labeled without transfection agents, and unless otherwise specified, the labeling was performed by incubating the cells with nanoparticles (200 μg mL^{-1}) for 4 h in a standard incubator unless specified. Labeled cells were then washed three times with sterile PBS to remove free particles.

SIO Labeling Conditions and Half-Life in hMSCs.

To optimize SIO labeling conditions, we performed two experiments that varied the labeling concentration and the labeling time. For the first experiment, cells were labeled with 0, 100, 200, 400, and 800 μg mL^{-1} of SIO for 4 h. For the second experiment, cells were labeled for 1, 2, 4, 6, 16, and 24 h at 200 μg mL^{-1}. Cells were then detached, counted, and analyzed for iron content by ICP-OES. To determine the half-life of SIO in hMSCs, we labeled cells at a concentration of 200 μg mL^{-1} for 4 h. Then, we plated 50 000 cells into four T25 flasks. On days 0, 1, 4, 7, and 14, cells were analyzed by ICP-OES for iron content.

Biocompatibility of SIO to hMSCs.

Cytotoxicity and proliferation assays were performed with a resazurin assay (Sigma-Aldrich). For cytotoxicity, cells were plated into a 96-well plate at a density of 10 000 cells/well and allowed to adhere overnight. Then, SIO (200 μL) at varying concentrations were added to the cells. After incubation for 72 h, the media with nanoparticles were removed and

cells were washed three times with PBS. Then, 10:1 v/v media/resazurin (100 uL) was added to all of the groups and allowed to incubate for 4 h. Fluorescence was then measured at excitation and emission wavelengths of 550 and 585 nm, respectively.

For proliferation, unlabeled and SIO-labeled hMSCs were plated at a density of 5000 cells cm^{-2} in 96-well plates. Viable cell numbers were then detected with the same resazurin assay on different days. The effect of SIO on hMSCs' viability was further confirmed with a calcein/EthD-III live/dead cell assay (Biotium). A positive control was created by adding CTAB (10%) to cells and incubating them for 4 h. All groups and an SIO-only control were analyzed with flow cytometry (FACSCanto 2, BD Biosciences).

The effect of SIO on cell differentiation were assessed *in vitro*. Unlabeled and SIO-labeled hMSCs were plated in a 6-well plate with approximately 70% confluency. Then the cells were treated with osteogenic and adipogenic induction media (PT-3002 and PT-3004, Lonza) with media changed every 3 days for 3 weeks. To better visualize the differentiation, adipogenic induced cells were stained with Oil Red O (Sigma-Aldrich), and osteogenic induced cells were stained with a von Kossa staining kit (Fisher Scientific). Control cells were treated with growth media. Stained cells were then observed with a microscope (BZ-X710, Keyence).

For the scratching/migration assay, cells were plated at a density of 5000 cells cm^{-2} and allowed to grow overnight. A line was then scratched with a pipet tip, leaving a gap between the cells. This area was then marked and imaged daily until the gap was completely refilled by migrating cells.

Phenotypes of hMSCs were detected by flow cytometry. First, unlabeled and SIO-labeled hMSCs were detached, centrifuged, and then resuspended in 100 μL of labeling buffer (PBS with 2 mM EDTA and 0.5% BSA) containing 10 μL of each antibody or isotype controls. The antibodies were selected for CD73-PE (clone AD2, 130–097-943, lot #5170202055), CD90-FITC (clone DG3, 130–097-930, lot #5170202054), and CD105-APC (clone 43A4E1, 130–099-125, lot #5170202046) from Miltenyi Biotech, and the isotypes were mouse IgG-PE, mouse IgG-FITC, and mouse IgG-APC (clone IS5–21F, Miltenyi Biotech).

The effect of SIO on cytokine secretion was studied by detecting cytokines in the cells culture media. SIO-labeled and unlabeled cells were plated at a density of 5000 cells cm^{-2} in a 6-well plate and allowed to incubate for 48 h. The media were then collected, and the cytokines in the media were analyzed with a Luminex human 62-plex (Human Immune Monitoring Center, Stanford University).

Long-Term Pro-survival Effect of IGF-Loaded SIO.

Cells were plated into a 96-well plate at a density of 9000 cells/well and allowed to grow for 2 days. The medium was then replaced with 100 μL of incomplete medium (MSCBM from Lonza) containing free IGF (200 ng mL^{-1}), free BSA (200 ng mL^{-1}), IGF-loaded SIO (562 μg mL^{-1}), or nothing. Three more control groups were included: cells with growth media (also known as complete media), incomplete media without cells, and IGF-loaded

nanoparticles without cells. Viable cell numbers were then detected with the resazurin assay (the same procedure with the cytotoxicity and proliferation assays) on days 1, 2, 4, and 7.

Magnet-Assisted Cell Direction and Retention.

To control the propagation of cells, SIO-labeled cells were detached and resuspended in 5 mL of growth media and added to T25 flasks. A magnet was taped on the outside of the flask's side wall. Control groups included SIO-labeled cells without an external magnet on the flask and unlabeled cells with an external magnet. The flasks were then put into the incubator overnight. The magnets were removed 2 days later. The area in the magnetic field was observed with a microscope (EVOS, Thermo Fisher Scientific) daily for 4 weeks. The flasks were held vertically except during the microscopic imaging.

We also investigated the cell retention under different shear stresses (7–35 dyn cm^{-2}) created with a peristaltic pump. Cells were loaded into the tube (inner diameter 0.86 mm) without passing the squeezing point. A magnet was then placed by the tube, and cells were observed under an EVOS microscope. Cells were stained with Qtracker 800 (Thermo Fisher Scientific) for better visualization. Then, the flow direction was reversed, and the cell solution was collected with different flow rates (2.8, 5.2, 8.5, 11.2, 13.0, and 14.6 mL min^{-1}). The cell concentration before and after the experiment was determined with a hemocytometer. Retention was calculated as (cell concentration before – cell concentration after)/cell concentration before.

In Vitro or *Ex Vivo* Ultrasound and Magnetic Resonance Imaging.

SIO or SIO-labeled hMSCs were suspended in 0.5% hot agarose solution at different concentrations of 0, 0.025, 0.05, 0.1, 0.2, 0.25, 0.4, 0.5, 2.5, and 5 mg mL^{-1} for nanoparticles or 0, 10 000, 50 000, 150 000, 300 000, and 600 000 cells/60 μL, injected into a 384-well plate while hot and then cooled before imaging. Ultrasound imaging of the phantom was performed with a 40-MHz-centered linear transducer (MS550) on a VEVO 2100 system (VisualSonics, Fujifilm). MR imaging was performed on a Bruker 7 T magnet with Avance II hardware, equipped with a 72 mm quadrature transmit/receive coil, and using a RAREVTR_T 2 series pulse sequence in ParaVision version 5.1. For T_2 measurements, the following parameters were used: TR = 5000 ms; TE = 12.6, 17.7, 62.8, 87.9, 113.0, 138.1, 163.2 ms; FOV (field of view) = 6.91 × 3.12 cm; slice thickness = 2 mm; and matrix size = 256 × 116. Relaxivities were calculated by linearly fitting plots of $1/T_2$ (s^{-1}) *versus* Fe ion concentrations (μM).

In Vivo Retention of SIO.

All animal studies were performed in accordance with the Institutional Animal Care and Use Committee (IACUC) at the University of California, San Diego (UCSD). Mice were anesthetized with 1–2% isoflurane. SIO in 50% Matrigel (40 μL of 10 mg mL^{-1}) were injected into the left ventricle myocardium close to the apex with a 31 gauge BD insulin syringe. The injection was guided by ultrasound imaging with a 40-MHz-centered linear transducer (MS550) on a VEVO 2100 system (VisualSonics, Fujifilm) in real time and assisted by an injection arm that came with the VEVO 2100 system. Immediately after the injection, the mouse was cleaned and a magnetic harness was put onto the mouse with the

magnet close to the heart apex. The harness was adjusted not to hinder normal movement of the animal, and the mouse was monitored twice daily. For the SIO control group, no magnetic harness was used on the animals. For the magnet control group, animals were put on magnetic harness but with no injections. After 7 days, the iron content in the hearts was determined with inductively coupled plasma mass spectrometry (iCAP RQ-ICP-MS, Thermo-Fisher). ICP-MS was used here because the concentration of the elements could be low and ICP-MS is more sensitive than ICP-OES.

Ischemia/Reperfusion Surgery.

C57B6 (12 weeks old) were anesthetized with a cocktail of ketamine (50 mg kg^{-1}) and xylazine (5 mg kg^{-1}) by i.p. injection for initial induction and then isoflurane (0.75–1.5%) for complete induction of anesthesia. Animals were ventilated throughout the entire procedure (PhysioSuite, Kent Scientific Co). With thoracotomy, LAD coronary artery occlusion was performed by tying an 8–0 prolene suture ligature on a piece of 2–0 silk suture. After 60 min of ischemia, 20 μL of 1:1 v/v DMEM/Matrigel or the same matrix containing unlabeled or IGF-loaded SIO-labeled hMSCs (5 million cells mL^{-1}) was injected intramyocardially below the ligation point close to the apex. All cells injected were passage number 5 from a same donor. Reperfusion was started by removing the 2–0 silk suture from around the LAD coronary artery. The chest was closed once the mouse was hemodynamically stable.

Ultrasound Imaging-Guided Intramyocardial Injection and Echocardiography.

For the ultrasound-guided intramyocardial injection, animals were anesthetized with 1–2% isoflurane and mounted to a warm animal bed with four contact electrode sensors for electrocardiography. A 40-MHz-centered linear transducer (MS550) on a VEVO 2100 system (VisualSonics, Fujifilm) was adjusted to show the parasternal long axis view of the heart and aligned with the syringe fixed on a mechanical injection assistant arm.

Animals for echocardiography were anesthetized with 0.25–1% isoflurane and underwent echocardiography using a VEVO 2100 ultrasound system (VisualSonics, SonoSite FUJIFILM) with a 40-MHz-centered linear transducer (MS550) as described previously.[36] The heart rate was controlled within 450 and 500 beats per minute. Cardiac function and structure were quantified *in vivo* by two-dimensional/speckle-tracking echocardiography by the software VEVO Lab (VisualSonics, Fujifilm). Ejection fraction (EF), GLS, and average peak strain values were determined and calculated as echocardiography-based parameters of LV contractility.

In Vivo Magnetic Resonance Imaging.

In vivo MR imaging was performed on a MRS4700 scanner with 4.7 T magnet (MR Solutions Ltd., UK). Animals were anesthetized with 1–2% isoflurane and immobilized on a mouse holder in a prone position during the scan. Scanning sequence cardiac IR segmented FLASH was used and the parameters were TR = 7 ms; TE = 2–64 ms; FOV (field of view) = 3.5 × 3.5 cm^2; slice thickness = 2 mm; and matrix size = 192 × 192. Electrocardiography and breath rate were gated for the imaging.

Histology.

Post mortem heart and body weights were measured, and hematoxylin/eosin-stained heart, lung, liver, and spleen tissue were studied. Cardiac interstitial fibrosis was evaluated on trichrome-stained sections. We quantified six random hearts from each group, and each heart was sectioned to 10 μm with every 10th section collected. We analyzed 4–13 slices for each group and calculated the percentage of fibrosis with four continuous slices that showed a maximum fibrosis and a coefficient of variation less than 15%. These sections were then scanned with a microscope under 40× magnification. For fibrosis quantification, fibrosis was calculated by count of blue pixels/count of blue and red pixels. The red and blue pixels were distinguished by changing the color threshold with ImageJ software, and the count of these pixels was measured. Color threshold settings for the entire heart (both red and blue pixels) was RGB color space with the triangle thresholding method. The fibrosis (blue pixels) was quantified with pixels with a hue between 150 and 195 by the triangle thresholding method. Heart sections were also stained with an iron staining kit from Sigma-Aldrich to visualize the SIO. The presence of injected hMSCs in the heart was evaluated by immunostaining for CD73-PE (clone REA804), CD90-FITC (clone REA897), and CD105-APC (clone 43A4E1) from Miltenyi Biotech.

Supplementary Material

Refer to Web version on PubMed Central for supplementary material.

ACKNOWLEDGMENTS

J.J. and F.C. acknowledge funding from the NIH R00 HL117048, DP2 HL137187, the Chancellor's Research Excellence Scholarships (4-G6), and infrastructure from S10 OD021821 and S10 OD18225. T.H. is grateful for the funding support by CSU (Grant No. 502041001). The authors also thank the American Cancer Society Institutional Research (Grant No. 14–250-42) provided through the Moores Cancer Center, University of California, San Diego. The authors would like to thank M. Farquhar for the use of the UCSD/CMM electron microscopy facility (supported by NIH equipment Grant No. 1S10OD023527–01), Y. Jones for electron microscopy sample preparation, P. Castillo and C. Maclsaac for the use of ICP-OES, and J. Rinehart for the use of SQUID. The authors also thank Y. Gu for ischemia/reperfusion surgery, Y. Chan for guidance on strain analysis, N. Dalton for manuscript editing, and J. Zhang for help with animal handling training. F.C. also acknowledges Y. Bai for strain analysis, C. Lin for help with cell collection and delivery, and C. Barback for MRI training. The authors are grateful to J. Olvera and C. Fine of the UCSD Human Embryonic Stem Cell Core Facility for technical assistance of flow cytometry experiments, which was made possible in part by the CIRM Major Facilities grant (FA1–00607) to the Sanford Consortium for Regenerative Medicine. Tissue Technology Shared Resource is supported by a National Cancer Institute Cancer Center Support Grant (CCSG Grant No. P30CA23100). This work was partially supported through access and utilization of the UC San Diego Department of Nanoengineering's Materials Research Center (NE-MRC). We also acknowledge the Signaling Gateway (funded by NIH/NIGM Grant No. 1 R01 GM078005–01) hosted by the San Diego Supercomputer Center at UCSD.

REFERENCES

(1). Forouzanfar MH; Moran AE; Flaxman AD; Roth G; Mensah GA; Ezzati M; Naghavi M; Murray CJ Assessing the Global Burden of Ischemic Heart Disease, Part 2: Analytic Methods and Estimates of the Global Epidemiology of Ischemic Heart Disease in 2010. Global Heart 2012, 7, 331–342. [PubMed: 23505617]

(2). Laflamme MA; Murry CE Heart Regeneration. Nature 2011, 473, 326–335. [PubMed: 21593865]

(3). Burridge PW; Sharma A; Wu JC Genetic and Epigenetic Regulation of Human Cardiac Reprogramming and Differentiation in Regenerative Medicine. Annu. Rev. Genet. 2015, 49, 461–484. [PubMed: 26631515]

(4). Lee RT; Walsh K The Future of Cardiovascular Regenerative Medicine. Circulation 2016, 133, 2618–2625. [PubMed: 27324357]

(5). Meyer GP; Wollert KC; Lotz J; Steffens J; Lippolt P; Fichtner S; Hecker H; Schaefer A; Arseniev L; Hertenstein B; et al. Intracoronary Bone Marrow Cell Transfer after Myocardial Infarction: Eighteen Months' Follow-up Data from the Randomized, Controlled Boost (Bone Marrow Transfer to Enhance St-Elevation Infarct Regeneration) Trial. Circulation 2006, 113, 1287–1294. [PubMed: 16520413]

(6). Lee RH; Pulin AA; Seo MJ; Kota DJ; Ylostalo J; Larson BL; Semprun-Prieto L; Delafontaine P; Prockop DJ Intravenous Hmscs Improve Myocardial Infarction in Mice Because Cells Embolized in Lung Are Activated to Secrete the Anti-Inflammatory Protein Tsg-6. Cell Stem Cell 2009, 5, 54–63. [PubMed: 19570514]

(7). Bolli R; Chugh AR; D'Amario D; Loughran JH; Stoddard MF; Ikram S; Beache GM; Wagner SG; Leri A; Hosoda T; Sanada F; Elmore JB; Goichberg P; Cappetta D; Solankhi NK; Fahsah I; Rokosh DG; Slaughter MS; Kajstura J; Anversa P Cardiac Stem Cells in Patients with Ischaemic Cardiomyopathy (Scipio): Initial Results of a Randomised Phase 1 Trial. Lancet 2011, 378, 1847–1857. [PubMed: 22088800]

(8). Hoover-Plow J; Gong Y Challenges for Heart Disease Stem Cell Therapy. Vasc. Health Risk Manage. 2012, 8, 99–113.

(9). Mohr A; Zwacka R The Future of Mesenchymal Stem Cell-Based Therapeutic Approaches for Cancer - from Cells to Ghosts. Cancer Lett. 2018, 414, 239–249. [PubMed: 29175461]

(10). Jokerst JV; Khademi C; Gambhir SS Intracellular Aggregation of Multimodal Silica Nanoparticles for Ultrasound-Guided Stem Cell Implantation. Sci. Transl. Med. 2013, 5, 177ra35.

(11). Nguyen PK; Lan F; Wang YM; Wu JC Imaging Guiding the Clinical Translation of Cardiac Stem Cell Therapy. Circ. Res. 2011, 109, 962–979. [PubMed: 21960727]

(12). Shen H; Cui G; Li Y; Ye W; Sun Y; Zhang Z; Li J; Xu G; Zeng X; Zhang Y; Zhang W; Huang Z; Chen W; Shen Z Follistatin-Like 1 Protects Mesenchymal Stem Cells from Hypoxic Damage and Enhances Their Therapeutic Efficacy in a Mouse Myocardial Infarction Model. Stem Cell Res. Ther. 2019, 10, 17–30. [PubMed: 30635025]

(13). Don CW; Murry CE Improving Survival and Efficacy of Pluripotent Stem Cell-Derived Cardiac Grafts. J. Cell. Mol. Med. 2013, 17, 1355–1362. [PubMed: 24118766]

(14). Christman KL; Vardanian AJ; Fang Q; Sievers RE; Fok HH; Lee RJ Injectable Fibrin Scaffold Improves Cell Transplant Survival, Reduces Infarct Expansion, and Induces Neovasculature Formation in Ischemic Myocardium. J. Am. Coll. Cardiol. 2004, 44, 654–660. [PubMed: 15358036]

(15). Kempen PJ; Greasley S; Parker KA; Campbell JL; Chang H-Y; Jones JR; Sinclair R; Gambhir SS; Jokerst JV Theranostic Mesoporous Silica Nanoparticles Biodegrade after Pro-Survival Drug Delivery and Ultrasound/Magnetic Resonance Imaging of Stem Cells. Theranostics 2015, 5, 631–642. [PubMed: 25825602]

(16). Cheng K; Li T-S; Malliaras K; Davis DR; Zhang Y; Marbán E Magnetic Targeting Enhances Engraftment and Functional Benefit of Iron-Labeled Cardiosphere-Derived Cells in Myocardial Infarction. Circ. Res. 2010, 106, 1570–1581. [PubMed: 20378859]

(17). Ottersbach A; Mykhaylyk O; Heidsieck A; Eberbeck D; Rieck S; Zimmermann K; Breitbach M; Engelbrecht B; Brügmann T; Hesse M; Welz A; Sasse P; Wenzel D; Plank C; Gleich B; Hölzel M; Bloch W; Pfeifer A; Fleischmann BK; Roell W Improved Heart Repair Upon Myocardial Infarction: Combination of Magnetic Nanoparticles and Tailored Magnets Strongly Increases Engraftment of Myocytes. Biomaterials 2018, 155, 176–190. [PubMed: 29179133]

(18). Moysidis SN; Alvarez-Delfin K; Peschansky VJ; Salero E; Weisman AD; Bartakova A; Raffa GA; Merkhofer RM; Kador KE; Kunzevitzky NJ; Goldberg JL Magnetic Field-Guided Cell Delivery with Nanoparticle-Loaded Human Corneal Endothelial Cells. Nanomedicine 2015, 11, 499–509. [PubMed: 25596075]

(19). Ruan J; Ji J; Song H; Qian Q; Wang K; Wang C; Cui D Fluorescent Magnetic Nanoparticle-Labeled Mesenchymal Stem Cells for Targeted Imaging and Hyperthermia Therapy of in Vivo Gastric Cancer. Nanoscale Res. Lett. 2012, 7, 309–320. [PubMed: 22709686]

(20). Zhu K; Li J; Wang Y; Lai H; Wang C Nanoparticles-Assisted Stem Cell Therapy for Ischemic Heart Disease. Stem Cells Int. 2016, 2016, 1384658–1384664. [PubMed: 26839552]

(21). Chen F; Ma M; Wang J; Wang F; Chern SX; Zhao ER; Jhunjhunwala A; Darmadi S; Chen H; Jokerst JV Exosome-Like Silica Nanoparticles: A Novel Ultrasound Contrast Agent for Stem Cell Imaging. Nanoscale 2017, 9, 402–411. [PubMed: 27924340]

(22). Tong CL; Eroglu E; Raston CL In Situ Synthesis of Phosphate Binding Mesocellular Siliceous Foams Impregnated with Iron Oxide Nanoparticles. RSC Adv. 2014, 4, 46718–46722.

(23). Lee SS; Riduan SN; Erathodiyil N; Lim J; Cheong JL; Cha J; Han Y; Ying JY Magnetic Nanoparticles Entrapped in Siliceous Mesocellular Foam: A New Catalyst Support. Chem. - Eur. J. 2012, 18, 7394–7403. [PubMed: 22588985]

(24). Schmidt-Winkel P; Lukens WW; Zhao D; Yang P; Chmelka BF; Stucky GD Mesocellular Siliceous Foams with Uniformly Sized Cells and Windows. J. Am. Chem. Soc. 1999, 121, 254–255.

(25). Qin Z; Joo J; Gu L; Sailor MJ Size Control of Porous Silicon Nanoparticles by Electrochemical Perforation Etching. Part. Part. Syst. Charact. 2014, 31, 252–256.

(26). Mascolo M; Pei Y; Ring T Room Temperature Co-Precipitation Synthesis of Magnetite Nanoparticles in a Large Ph Window with Different Bases. Materials 2013, 6, 5549–5567. [PubMed: 28788408]

(27). Gu L; Park J-H; Duong KH; Ruoslahti E; Sailor MJ Magnetic Luminescent Porous Silicon Microparticles for Localized Delivery of Molecular Drug Payloads. Small 2010, 6, 2546–2552. [PubMed: 20814923]

(28). Zhang HY; Dunphy DR; Jiang XM; Meng H; Sun BB; Tarn D; Xue M; Wang X; Lin SJ; Ji ZX; Li RB; Garcia FL; Yang J; Kirk ML; Xia T; Zink JI; Nel A; Brinker CJ Processing Pathway Dependence of Amorphous Silica Nanoparticle Toxicity: Colloidal Vs Pyrolytic. J. Am. Chem. Soc. 2012, 134, 15790–15804. [PubMed: 22924492]

(29). Zhu Y Modern Techniques for Characterizing Magnetic Materials; Springer Science & Business Media: New York, 2005.

(30). Sunday KJ Development of Ferrite-Coated Soft Magnetic Composites: Correlation of Microstructure to Magnetic Properties. Ph.D. Thesis, Drexel University, Philadelphia, 2017.

(31). Kolhatkar AG; Jamison AC; Litvinov D; Willson RC; Lee TR Tuning the Magnetic Properties of Nanoparticles. Int. J. Mol. Sci. 2013, 14, 15977–16009. [PubMed: 23912237]

(32). Nidhin M; Indumathy R; Sreeram K; Nair BU Synthesis of Iron Oxide Nanoparticles of Narrow Size Distribution on Polysaccharide Templates. Bull. Mater. Sci. 2008, 31, 93–96.

(33). Doherty GJ; McMahon HT Mechanisms of Endocytosis. Annu. Rev. Biochem. 2009, 78, 857–902. [PubMed: 19317650]

(34). Chen F; Li G; Zhao ER; Li J; Hableel G; Lemaster JE; Bai Y; Sen GL; Jokerst JV Cellular Toxicity of Silicon Carbide Nanomaterials as a Function of Morphology. Biomaterials 2018, 179, 60–70. [PubMed: 29980075]

(35). Gaharwar AK; Mihaila SM; Swami A; Patel A; Sant S; Reis RL; Marques AP; Gomes ME; Khademhosseini A Bioactive Silicate Nanoplatelets for Osteogenic Differentiation of Human Mesenchymal Stem Cells. Adv. Mater. 2013, 25, 3329–3336. [PubMed: 23670944]

(36). Kim T; Lemaster JE; Chen F; Li J; Jokerst JV Photoacoustic Imaging of Human Mesenchymal Stem Cells Labeled with Prussian Blue-Poly(L-Lysine) Nanocomplexes. ACS Nano 2017, 11, 9022–9032. [PubMed: 28759195]

(37). Rodriguez-Porcel M; Gheysens O; Chen IY; Wu JC; Gambhir SS Image-Guided Cardiac Cell Delivery Using High-Resolution Small-Animal Ultrasound. Mol. Ther. 2005, 12, 1142–1147. [PubMed: 16111921]

(38). Tong S; Hou S; Zheng Z; Zhou J; Bao G Coating Optimization of Superparamagnetic Iron Oxide Nanoparticles for High T2 Relaxivity. Nano Lett. 2010, 10, 4607–4613. [PubMed: 20939602]

(39). Lee N; Kim H; Choi SH; Park M; Kim D; Kim H-C; Choi Y; Lin S; Kim BH; Jung HS; Kim H; Park KS; Moon WK; Hyeon T Magnetosome-Like Ferrimagnetic Iron Oxide Nanocubes for Highly Sensitive Mri of Single Cells and Transplanted Pancreatic Islets. Proc. Natl. Acad. Sci. U. S. A. 2011, 108, 2662–2667. [PubMed: 21282616]

(40). Xie X; Shen Y; Chen J; Huang Z; Ge J Mineralocorticoid Receptor Deficiency Improves the Therapeutic Effects of Mesenchymal Stem Cells for Myocardial Infarction *Via* Enhanced Cell Survival. J. Cell. Mol. Med. 2018, 23, 1246–1256. [PubMed: 30549184]

(41). Schmidt MB; Chen EH; Lynch SE A Review of the Effects of Insulin-Like Growth Factor and Platelet Derived Growth Factor on *in Vivo* Cartilage Healing and Repair. Osteoarthritis Cartilage 2006, 14, 403–412. [PubMed: 16413799]

(42). Pervin F; Chen WW Mechanically Similar Gel Simulants for Brain Tissues. Dynamic Behavior of Materials 2011, 1, 9–13.

(43). Chiu J-J; Chien S Effects of Disturbed Flow on Vascular Endothelium: Pathophysiological Basis and Clinical Perspectives. Physiol. Rev. 2011, 91, 327–387. [PubMed: 21248169]

(44). Jiang Y; Kohara K; Hiwada K Low Wall Shear Stress in Carotid Arteries in Subjects with Left Ventricular Hypertrophy. Am. J. Hypertens. 2000, 13, 892–898. [PubMed: 10950397]

(45). Yamada S; Arrell DK; Martinez-Fernandez A; Behfar A; Kane GC; Perez-Terzic CM; Crespo-Diaz RJ; McDonald RJ; Wyles SP; Zlatkovic-Lindor J; Nelson TJ; Terzic A Regenerative Therapy Prevents Heart Failure Progression in Dyssynchronous Nonischemic Narrow Qrs Cardiomyopathy. J. Am. Heart Assoc. 2015, 4, No. e001614. [PubMed: 25964205]

(46). Xiao Y-F; Min J-Y; Morgan JP Immunosuppression and Xenotransplantation of Cells for Cardiac Repair. Annals of Thoracic Surgery 2004, 77, 737–744.

(47). Golpanian S; Schulman IH; Ebert RF; Heldman AW; DiFede DL; Yang PC; Wu JC; Bolli R; Perin EC; Moye L; Simari RD; Wolf A; Hare JM Concise Review: Review and Perspective of Cell Dosage and Routes of Administration from Preclinical and Clinical Studies of Stem Cell Therapy for Heart Disease. Stem Cells Transl. Med. 2016, 5, 186–191. [PubMed: 26683870]

(48). Nguyen PK; Rhee JW; Wu JC Adult Stem Cell Therapy and Heart Failure, 2000 to 2016 a Systematic Review. Jama Cardiology 2016, 1, 831–841. [PubMed: 27557438]

(49). Reisner SA; Lysyansky P; Agmon Y; Mutlak D; Lessick J; Friedman Z Global Longitudinal Strain: A Novel Index of Left Ventricular Systolic Function. Journal of the American Society of Echocardiography 2004, 17, 630–633. [PubMed: 15163933]

(50). Ottersbach A; Mykhaylyk O; Heidsieck A; Eberbeck D; Rieck S; Zimmermann K; Breitbach M; Engelbrecht B; Brugmann T; Hesse M; Welz A; Sasse P; Wenzel D; Plank C; Gleich B; Holzel M; Bloch W; Pfeifer A; Fleischmann BK; Roell W Improved Heart Repair Upon Myocardial Infarction: Combination of Magnetic Nanoparticles and Tailored Magnets Strongly Increases Engraftment of Myocytes. Biomaterials 2018, 155, 176–190. [PubMed: 29179133]

(51). Hanahan D; Weinberg RA The Hallmarks of Cancer. Cell 2000, 100, 57–70. [PubMed: 10647931]

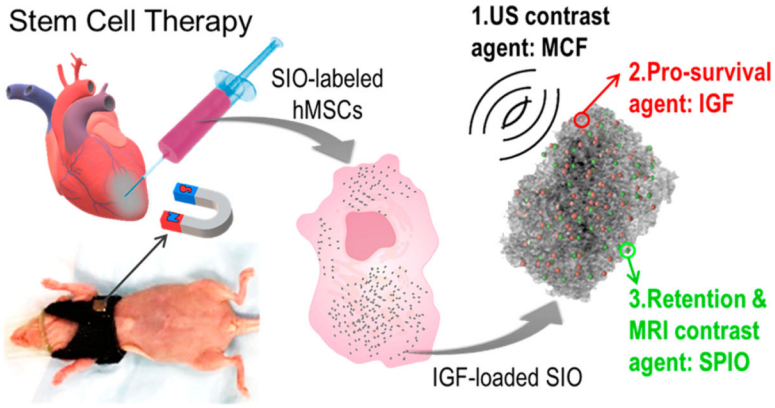

Figure 1.

Schematic of treatment approach with multifunctional silica–iron oxide nanoparticles (SIO). The SIO increase ultrasound (US) and magnetic resonance imaging (MRI) contrast of human mesenchymal stem cells (hMSCs). They can also increase cell retention *via* the iron oxide nanoparticles embedded in the silica and an external magnet. Moreover, the SIO improve cell viability with sustained release of insulin-like growth factor (IGF).

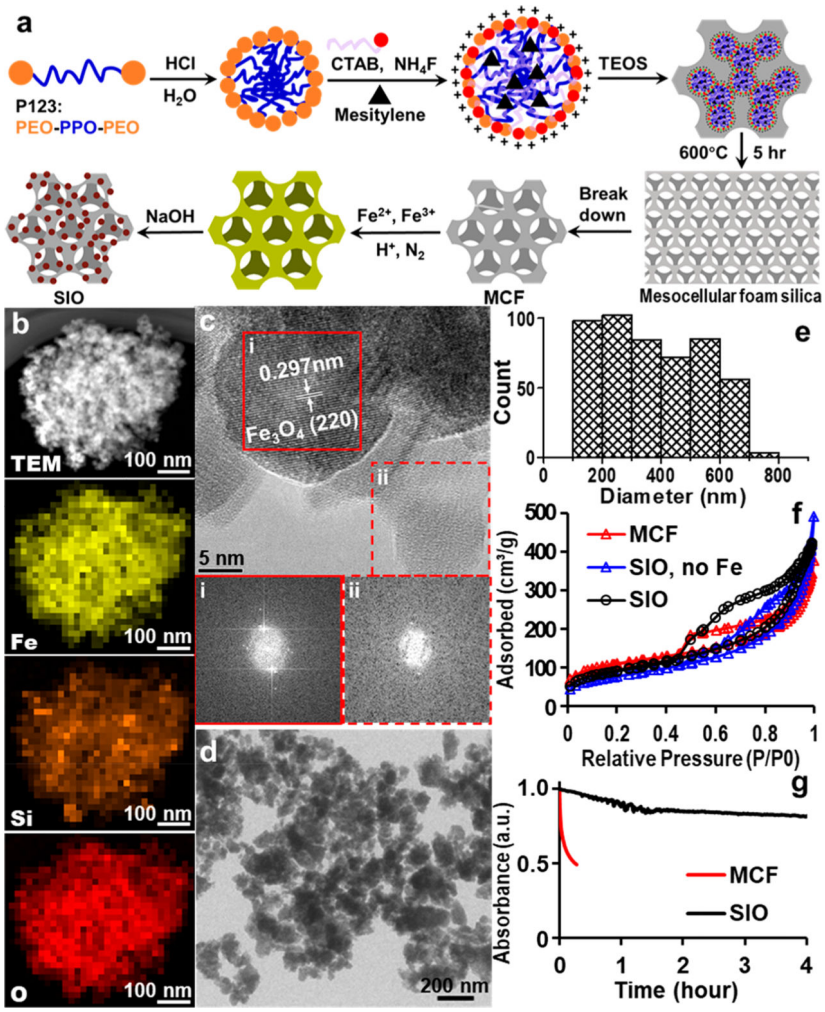

Figure 2.

SIO synthesis, optimization, and characterization. (a) Schematic synthesis of SIO. SPIO were grown *in situ* on calcined MCF prepared by a micelle-templated sol–gel method. (b) TEM image and EDX element mapping of a representative SIO. The mapping shows that the iron is well-dispersed in the MCF. (c) HRTEM analysis indicates the presence of both crystal and amorphous regions. The lattice spacing of panel i is about 2.97 Å, which agrees well with the lattice spacing of (220) planes of cubic Fe_3O_4. Below the HRTEM image, the fast Fourier transformation (FFT) patterns confirm the crystalline and amorphous features of panels i and ii. The amorphous structure is typically found in silica nanoparticles made with low-temperature sol–gel method,[24] sonication, and gradient centrifuge.[25] (d) Low-magnification TEM image of multiple SIO shows that SIO were irregularly shaped. (e) TEM size distribution of the SIO. The average size of SIO is 380 nm. The diameter is the average of Feret and MinFeret measured by ImageJ. Feret diameter is the longest distance between any two points along the selection boundary, also known as the maximum caliper. MinFeret diameter is the shortest distance along the longest axis, *i.e.*, short axis of a ellipse. (f) Nitrogen adsorption–desorption analysis indicates that both MCF and SIO were mesoporous. We also tested a product with catalyst but no iron precursors (SIO, no Fe).

Increased pore volume and pore size in this product indicates the dissolution of silica during *in situ* growth. (g) Deposition of SPIO increased the colloidal stability of SIO compared to the MCF. The absorbances were normalized to the first time point.

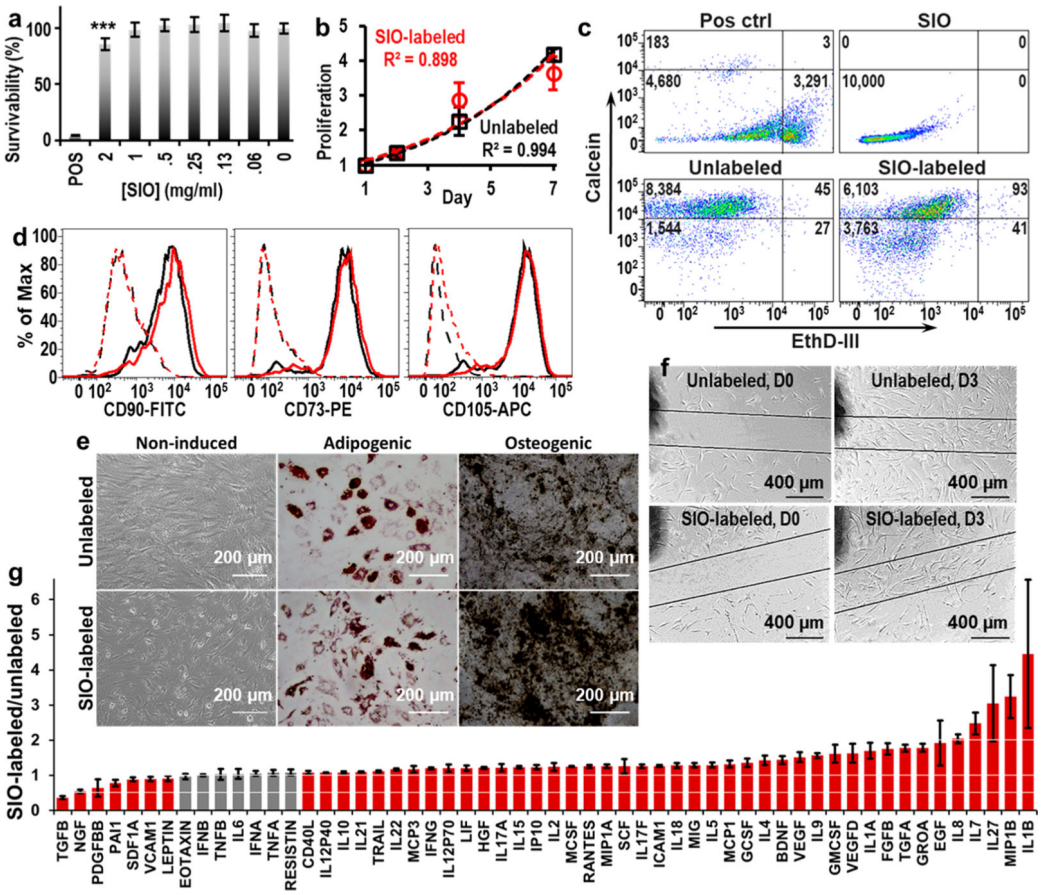

Figure 3.

Biocompatibility of SIO to hMSCs. (a) Resazurin assay showed no significant decrease in cell viability at SIO concentrations below 1 mg/mL. Error bars are standard deviations of six replicates; ***$p < 0.0005$. (b) Exponential fitting curves for proliferation of SIO-labeled and unlabeled hMSCs are similar, and the doubling times for SIO-labeled and unlabeled hMSCs were 3.6 and 3.7 days. Error bars are standard deviations of eight replicates. (c) Calcein/ethidium homodimer III live/dead assay shows that only 0.4% of cells died after being labeled with SIO. (d) Flow cytometry showed SIO-labeled hMSCs maintained the phenotypes—CD73, CD90, and CD105. Black and red lines are unlabeled and SIO-labeled hMSCs, respectively. Dashed lines are isotype control with isotype mouse IgG; solid lines are hMSCs stained with specific binding antibodies. (e) SIO-labeled hMSCs maintained their adipogenic and osteogenic differentiation ability. (f) SIO-labeled hMSCs showed normal migration. (g) Fold change of cytokines secreted by SIO-labeled and unlabeled hMSCs. SIO-labeled hMSCs secreted more than 200% of IL1B, IL27, IL7, IL8, and MIP1B and less than 50% of TGFB than unlabeled ones. Gray bars indicate a statistically nonsignificant ($p > 0.05$) change in expression; red bars indicate significance ($p < 0.05$) for the two-tailed homoscedastic test. Error bars are standard deviation of four replicates.

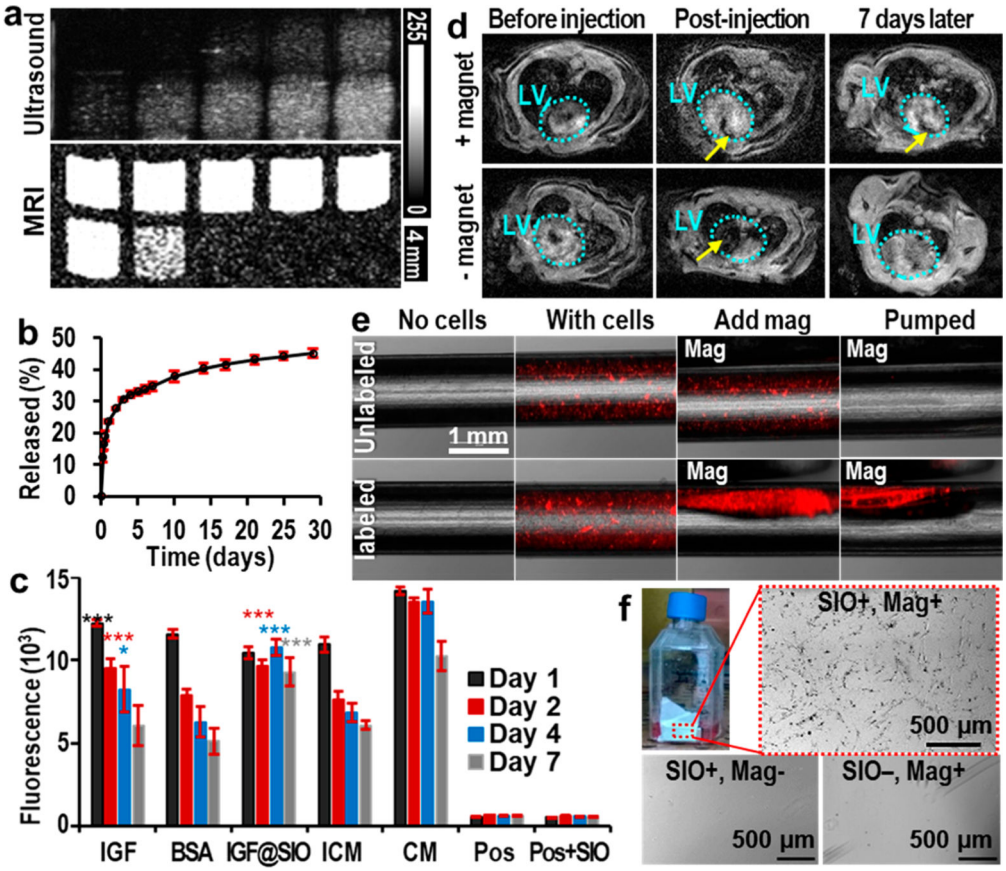

Figure 4.

Multiple functions of SIO. (a) Ultrasound and T_2-weighted MR images of unlabeled (top row, the cell numbers are 0k, 10k, 50k, 150k, and 300k from left to right) and SIO-labeled hMSCs (bottom row, the cell numbers are 10k, 50k, 150k, 300k, and 600k from left to right). These images show the enhancement of both MRI and ultrasound signals of hMSCs after SIO labeling. MRI was done with a repetition time of 1400 ms and an echo time of 15 ms at 4.7 T. (b) Cumulative release profile of IGF from SIO. Error bars are standard deviations of triplicates. (c) *In vitro* survival of hMSCs treated with free IGF, free BSA, IGF-loaded SIO (IGF@SIO), incomplete media (ICM), and complete media (CM). No cells and nanoparticle-only groups are control groups with only incomplete media or media containing nanoparticles. Error bars are standard deviations of six replicates. The asterisks show the p value compared to incomplete media group; $*p < 0.05$, $***p < 0.0005$. (d) MRI shows the long-term retention of SIO in the left ventricle wall only with the presence of a magnet. Azure dotted circles show the outlines of the left ventricles. Yellow arrows indicate the locations of SIO. (e) Overlay of fluorescence and microscope images show that SIO and magnets could improve the retention of hMSCs in laminar flow with a shear stress at 27 dyn/cm^2. Both cells were stained with fluorescent quantum dots for visualization. (f) Suspended SIO-labeled hMSCs could be directed by an external magnet to the side wall of the flask. These attracted cells could adhere to and grow on the side wall. In contrast, no cells would grow on the same location without SIO labeling or without a magnet.

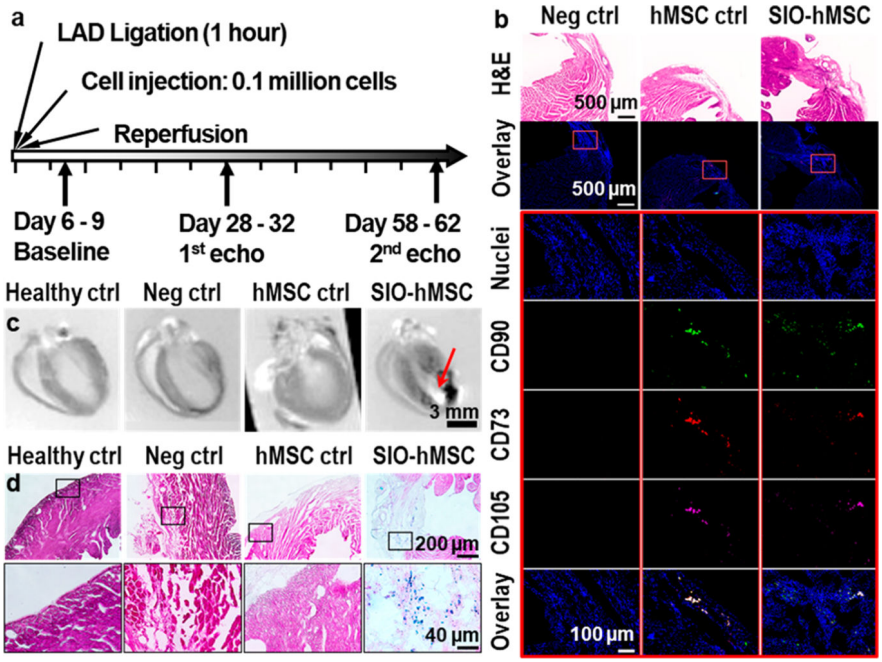

Figure 5.

Timeline and confirmation of treatments in myocardium after 60 days. (a) Timeline for surgery, treatment, and echocardiograph. Hearts were collected and sliced more than 60 days after injection of hMSCs. (b) H&E staining (first row) and immunofluorescence (second row) images of heart slices from the injured groups. The third to seventh rows show higher-magnification images of the outlined regions (highlighted with red rectangles) from the second row. The results indicated the presence of hMSCs' phenotypes CD73, CD90, and CD105 in heart slices from both hMSC control and IGF-loaded SIO-labeled hMSCs. (c) *Ex vivo* MRI showed the presence of SIO (pointed by red arrow) only in the IGF-loaded SIO-labeled hMSC treatment group. (d) Iron staining of heart slices from each group. Iron was stained blue; myocardium cells were stained dark pink, and fibrosis was stained light pink. The result shows the presence of iron only in the IGF-loaded SIO-labeled hMSCs treatment group.

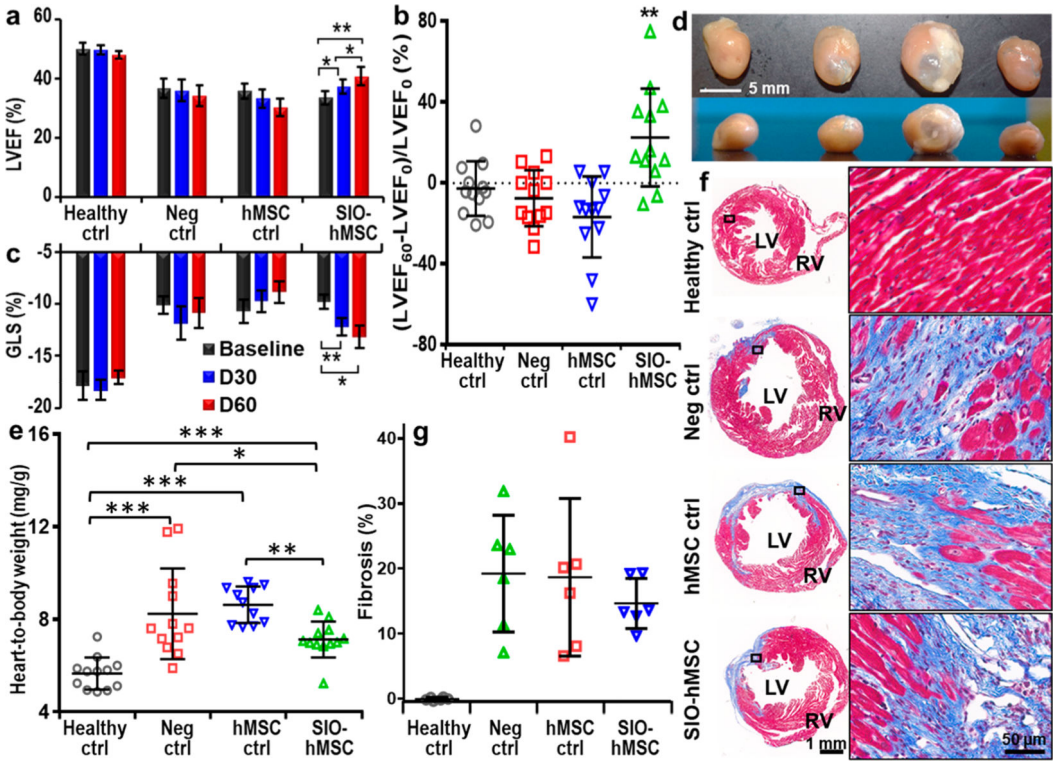

Figure 6.

Effects of IGF-loaded SIO-labeled hMSC treatment on cardiac functions and pathological evaluation. (a) Comparison of mean LVEF among four groups ($n = 12$) from baseline, day 30, and day 60. IGF-loaded SIO-labeled hMSCs significantly increased LVEF and absolute value of global longitudinal strain (GLS) on both day 30 and 60 compared to the baseline. Error bars are standard errors ($n = 12$); *$p < 0.05$, **$p < 0.005$. (b) Change of LVEF on day 60 from baseline for individual subjects. Error bars are standard deviations ($n = 12$); **$p < 0.005$ (two-tail and type-two t test was used). (c) Mean GLS of each group ($n = 12$) from baseline, day 30, and day 60. (d) Photos show frontal view (top row) and transverse view (bottom row) of a representative heart from each group. (e) Mean heart-to-body weight ratio of each group. Error bars are standard errors ($n = 11$ for hMSC control group and 12 for the other three groups); *$p < 0.05$, **$p < 0.005$, ***$p < 0.0005$. (f) Representative heart slices stained with trichrome staining from each group. Blue indicates fibrosis, and red indicates myocardium. RV: right ventricle. (g) Quantitative analysis for fibrosis. Error bars are standard deviations for six animals.